Materials Science and Engineering: A Volume 700, 17 July 2017, Pages 291-300

Enhancement of mechanical properties in high silicon gravity cast AlSi9Mg alloy refined by Al3Ti3B master alloy

Xixi Dong, Yijie Zhang, Shouxun Ji

Abstract

The microstructure and mechanical properties of high silicon Al9Si0.45Mg alloys without grain refinement and refined by Al5Ti1B and Al3Ti3B master alloys were investigated. The results showed that the primary α–Al grain sizes were 1288 ± 361 μm and 645 ± 146 μm in the non–refined and Al5Ti1B refined alloys respectively, and that was decreased significantly to 326 ± 116 μm in Al3Ti3B refined alloy. After T6 heat treatment, the yield strength, ultimate tensile strength and elongation of the non–refined alloy were 298 ± 2 MPa, 350 ± 2 MPa and 4.5 ± 0.7% separately. When the grain refiner was changed from Al5Ti1B to Al3Ti3B, the yield strength was increased from 304 ± 2 MPa to 311 ± 1 MPa, the ultimate tensile strength was increased from 357 ± 3 MPa to 366 ± 1 MPa, and the elongation was increased significantly by 38.8% from 8.0 ± 1.0% to 11.1 ± 1.2%. The Hall–Petch relation between the yield strength and grain size of the heat–treated alloys was determined as $\sigma y = 285.1 + 470.2 \cdot d^{-1/2}$. It was found that β" phase was precipitated from the α–Al matrix for the peak strengthening of the heat–treated alloys. TiB2 and TiAl3 particles were found coexisting in Al5Ti1B master alloy, while TiB2 and AlB2 particles were verified coexisting in Al3Ti3B master alloy. The inoculation of AlB2 particles results in the significant grain refinement under Al3Ti3B. The increase of strength in the Al3Ti3B refined alloy is attributed to the refinement of the primary α–Al grains, while the increase of ductility in the Al3Ti3B refined alloy resulted from the reduced oxides and porosity defects as well as decreased grain size.

Keywords

Aluminium alloys; Microstructure; Mechanical properties; High silicon; Grain refinement; Precipitation strengthening

1. Introduction

Al–Si–Mg cast alloys have been widely used for making high integrity castings with a combination of good castability, strength, ductility and corrosion resistance [1–3], which are necessary for transport manufacturing to provide light weighting components. The most commonly used Al–Si–Mg cast alloy with good ductility is A356, which contains 6.5–7.5 wt% Si, 0.3–0.45 wt% Mg and provides a yield strength up to 280 MPa [4,5]. However, recent developments in manufacturing lightweight components require the aluminium cast alloys to be able to provide higher strength and also good ductility.

Generally, the strengthening mechanisms in aluminium cast alloys include grain size/grain boundary strengthening, secondary phase strengthening, solution strengthening, precipitate strengthening and strain strengthening. The increase of Si and Mg contents can increase the amount of secondary eutectic Si phase and the Mg2Si precipitate phase. Therefore, on the basis of A356 alloy, it is expected that the increase of Si level to 9 wt% with the Mg content kept at the up level of 0.45 wt% could offer a higher strength Al–Si–Mg alloy, without obvious decreasing the ductility, since the porosity could be decreased due to the increase of castability. Therefore, it is interesting to study the high silicon Al9Si0.45Mg cast alloys.

Grain refinement has been proved as an important melt treatment during casting aluminium alloys in order to obtain fine primary α–Al grains, which can improve the toughness, strength, formability and machinability [6–9]. Al–Ti–B master alloys, in particular Al5Ti1B, have been widely used as grain refiners over the past several decades [10,11]. The Al5Ti1B master alloy offers a remarkable performance in the casting of wrought alloys, but it is hard to meet the expectations in the case of cast Al–Si alloys, especially with a content of Si higher than 7 wt% [6,12]. The reason is that Si in the melt reacts with Ti to form Ti–Si phases, which poison the TiB2 nucleation sites and consumes the Ti dissolved in the melt for grain growth restriction [12,13]. Thus the decrease of grain refining efficiency under the commonly used Al5Ti1B master alloy is a severe problem for the high silicon Al9Si0.45Mg cast alloy. One effective method is to reduce the Ti content and increase the B content in the master alloys, and some new master alloys such as Al3Ti3B and Al3Ti1B have been reported, among which Al3Ti3B was found to be able to provide effective grain refinement [14–18]. Therefore, Al3Ti3B master alloy could be considered as a solution to overcome the grain refining problem accompanied with the high silicon Al9Si0.45Mg cast alloy.

The objectives of this paper are to assess the effects of Al5Ti1B and Al3Ti3B grain refiners on the microstructure, and mechanical properties of the high silicon Al9Si0.45Mg cast alloy, to shed a light on the solution of the grain refinement problem accompanied with the high silicon cast aluminium alloy, and provide high strength cast aluminium alloys with high castability, good ductility and excellent corrosion resistance, to meet the increasing requirements in automotive industry.

2. Experimental

2.1. Materials and melt preparation

The base alloy A0, with the composition listed in Table 1 and in the form of ingot, was melted in three 12-kg capacity clay–graphite crucibles separately using an electric resistance furnace. The alloying elements were added to the melt of A0 in order to adjust it to the desired compositions of A1, A2 and A3, as listed in Table 1, where magnesium was added in the pure ingot, and silicon was added in the form of Al–50 wt% Si master alloys. During melting, the temperature of the furnace was controlled at 750 °C, and a melt of 8 kg was prepared in each of the three crucibles. After one hour of homogenisation, Al–10 wt% Sr master alloy was added into the melt to make the defined Sr content of 120 ppm, for modifying the morphology of the eutectic silicon phase during solidification. The melt was subsequently degassed through injecting pure argon into the melt by using a rotary degassing impeller at a speed of 350 rpm

for 4 min. After degassing, the top surface of the melt was covered by commercial granular flux, and the melt was hold for 10 min for temperature recovery, followed by casting without grain refinement (GR) using the melt in one crucible, or adding 0.2 wt% Al5Ti1B or 0.2 wt% Al3Ti3B master alloys into the melt in the other two crucibles separately for grain refinement. After adding the grain refiner, the melt was stirred and then hold for 10 min before casting. Mushroom samples were made for composition analysis. The chemical compositions of the alloys were measured by inductively coupled plasma atomic emission spectroscopy (ICP–AES), and the results are listed in Table 1.

Table 1. Chemical compositions of experimental alloys analyzed by ICP–AES (wt%).

Alloy	Si	Mg	Cu	Fe	Mn	Ti	Sr	B	Al
A0 (Al8.3Si0.31Mg)	8.31	0.31	0.00	0.11	0.06	0.130	0.000	0.000	Bal.
A1(Al9Si0.45Mg+No GR)	8.84	0.45	0.00	0.11	0.06	0.130	0.012	0.000	Bal.
A2(Al9Si0.45Mg+Al5Ti1B)	8.80	0.45	0.00	0.11	0.06	0.140	0.012	0.002	Bal.
A3(Al9Si0.45Mg+Al3Ti3B)	8.82	0.45	0.00	0.11	0.06	0.135	0.012	0.006	Bal.

2.2. Casting process and heat treatment

With the intention of casting tensile test bars, the prepared melt was poured at 720 ℃ into a keel block permanent mould preheated at 460 ℃, as shown in Fig. 1(a). Fig. 1(b) shows the gravity casting made by the permanent mould, and one round tensile test bar with a size of ϕ20 mm × 166 mm was made from each casting, as indicated by the dashed rectangle box in Fig. 1(b). Eight castings were made one after one in 20 min for each of the non–refined, Al5Ti1B refined and Al3Ti3B refined condition. After kept at ambient condition for at least 24 h, the cast tensile test bars were subjected to T6 heat treatment in an electrical furnace equipped with forced air circulation, including solution treatment and artificial aging. Solution treatment was carried out at 540 °C for 8 h, followed by immediate water quenching to room temperature. Aging treatment was performed at 170 °C for 8 h, followed by air cooling to room temperature. The T6 heat–treated tensile test bars were then machined into the shape shown in Fig. 1(c) for tensile tests, with the gauge dimension of ϕ10 mm × 50 mm.

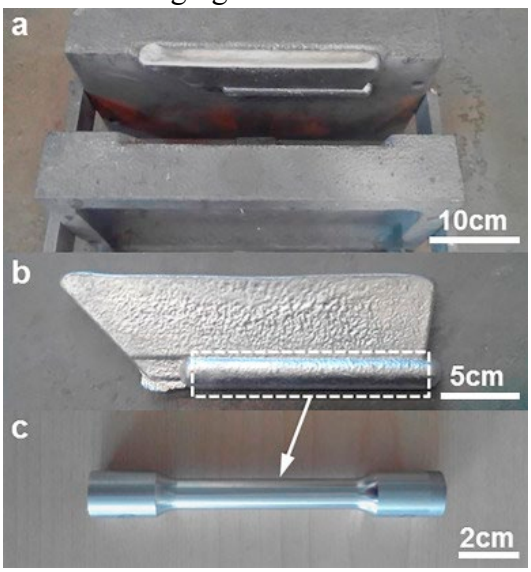

Fig. 1. (a) Keel block permanent casting mould, (b) gravity casting made by the mould and (c) machined tensile test bar from the casting.

2.3. Tensile tests and characterization

Tensile tests were conducted following the ASTM B557 standard using an Instron 5500 Universal Electromechanical Testing System. All the tensile tests were performed at room temperature. The gauge length of the extensometer was 50 mm and the ramp rate for extension was 1 mm/min. Each data reported with standard deviation was based on the mechanical properties obtained from 6 to 8 samples. The microstructure was examined using the Zeiss optical microscopy (OM), the Zeiss SUPRA 35VP scanning electron microscope (SEM) equipped with energy dispersive X-ray spectroscopy (EDS), the JEOL–2100 transmission electron microscopy (TEM) and the D8 X–ray diffraction (XRD) instrument. The specimens for OM, SEM and XRD analysis were prepared by the standard technique of grinding. OM observation was conducted after polishing without any etching. Polarized OM observation of grain size was performed after anodised with Barker solution (97 vol% H2O and 3 vol% HBF4). Porosity area percentage was counted from the longitudinal section of three as–cast bars. SEM analysis was conducted after etching with 15 vol% HCl. Post–loading fracture analysis was also performed via SEM. Thin specimens for TEM observation were prepared by standard electropolishing. The electrolytic solution was a mixture of nitric acid and methyl alcohol (2:8), used at －20 to －30 ℃ and 20 V. TEM operating at 200 kV was used for bright field imaging, select area diffraction pattern (SADP) analysis, and high－resolution transmission electron microscopy (HRTEM) imaging. XRD analysis was conducted from 2 Theta degrees 25° to 100° at a scanning speed of 1°/min.

3. Results

3.1. As–cast microstructure

Fig. 2(a) and (b) show the OM morphology of the as–cast Al9Si0.45Mg alloys refined by Al5Ti1B and Al3Ti3B, respectively. The primary α–Al phase in the Al5Ti1B refined alloy shows coarse dendrite morphology, while the primary α–Al phase in the Al3Ti3B refined alloy shows fine dendrite morphology. The primary α–Al phase refined by Al3Ti3B is much finer than that refined by Al5Ti1B. Moreover, no coarse plate–like eutectic Si phase was observed in the as–cast alloys, which indicated that the eutectic Si phase was well modified.

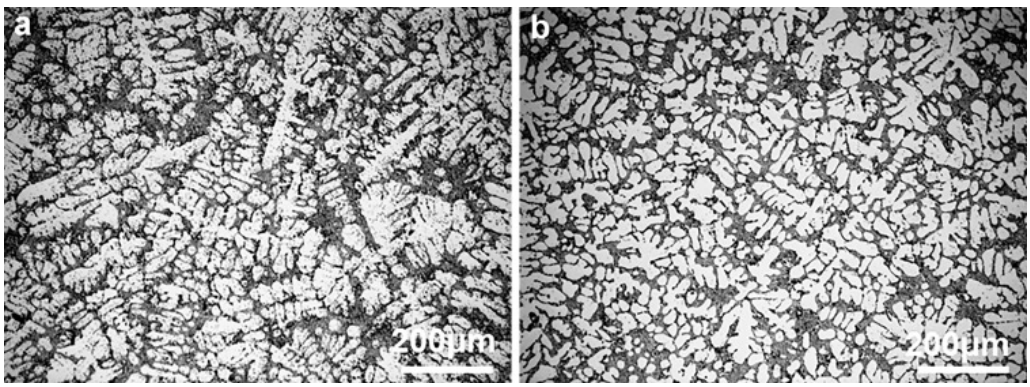

Fig. 2. Optical micrographs showing the morphology of the as–cast Al9Si0.45Mg alloys refined by (a) Al5Ti1B and (b) Al3Ti3B.

Fig. 3(a), (b) and (c) present the polarized optical micrographs showing the grain size of primary α–Al phase in the as–cast Al9Si0.45Mg alloys without grain refinement and refined by Al5Ti1B and Al3Ti3B master alloys, respectively. The primary α–Al phase shows coarse dendritic morphology in the as–cast Al9Si0.45Mg0.4Cu alloy without grain refinement and refined by Al5Ti1B. The primary α–Al phase in the as–cast Al9Si0.45Mg alloy refined by Al3Ti3B is significantly finer than the non–refined and Al5Ti1B refined condition. Fig. 3(d) and (e) show the statistical distribution of grain size and statistical average grain size of primary α–Al phase in the as–cast Al9Si0.45Mg alloys under the three grain refinement condition, separately. From Fig. 3(d), the grain size shows lognormal distribution, and the majority of the primary α–Al phase in the Al3Ti3B refined alloy is much finer than that in the non–refined and Al5Ti1B refined alloys. From Fig. 3(e), the grain size of the primary α–Al phase is 1288 ± 361 μm without grain refinement, and that is 645 ± 146 μm when refined by Al5Ti1B, while that is 326 ± 116 μm when refined by Al3Ti3B. The grain size of primary α–Al phase in the Al3Ti3B refined alloy is reduced by 49.5%, when compared with the Al5Ti1B refined alloy. It could be confirmed that Al3Ti3B is more effective grain refiner for the high silicon Al9Si0.45Mg cast alloy than Al5Ti1B.

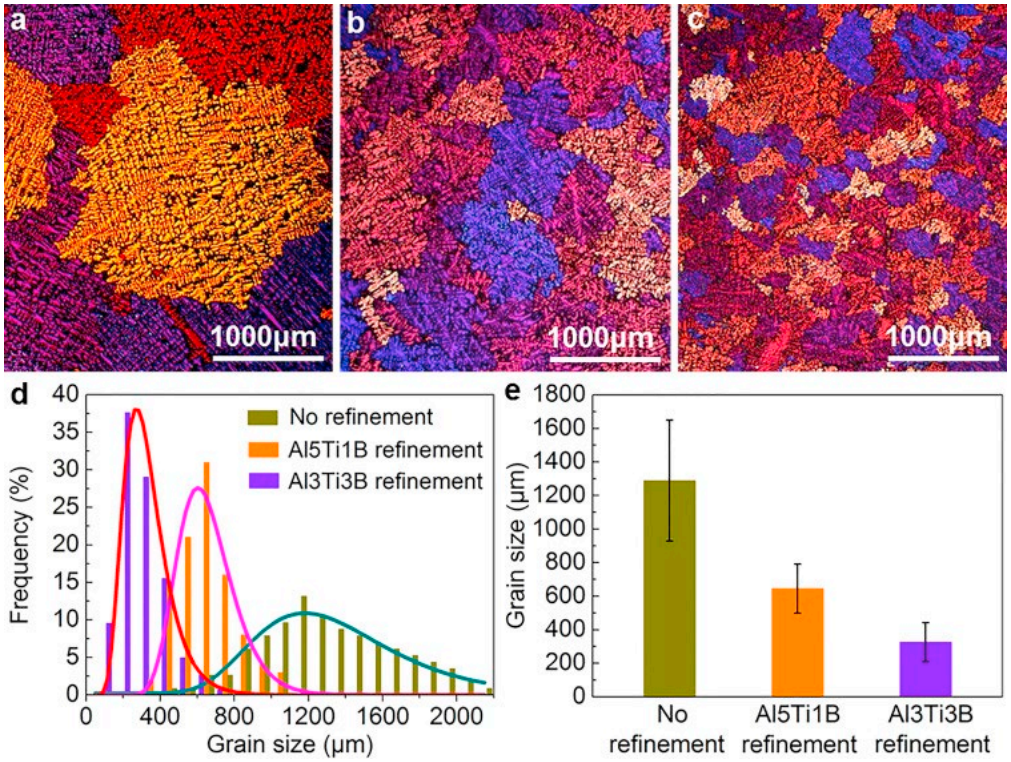

Fig. 3. Polarized optical micrographs showing the grain size of primary α–Al phase in the as–cast Al9Si0.45Mg alloys refined by (a) No refinement, (b) Al5Ti1B, (c) Al3Ti3B, and (d) statistical distribution of grain size and (e) statistical average grain size.

Fig. 4(a) and (b) show the SEM micrographs of the isolated eutectic Si phase in the as–cast Al9Si0.45Mg alloys refined by Al5Ti1B and Al3Ti3B respectively, after deep etching. The eutectic Si phase was properly modified to fine fibrous structure with small aspect ratios, as

indicated by arrows in Fig. 4. The eutectic Si phase in unmodified Al–Si alloys has been reported as coarse plate–like structure with high aspect ratio that could be over 27 [19], which is prone to induce crack under loading. The refined eutectic Si fibres are desirable to obtain a fine microstructure after solution treatment, and it could be beneficial to the mechanical properties especially ductility after heat treatment.

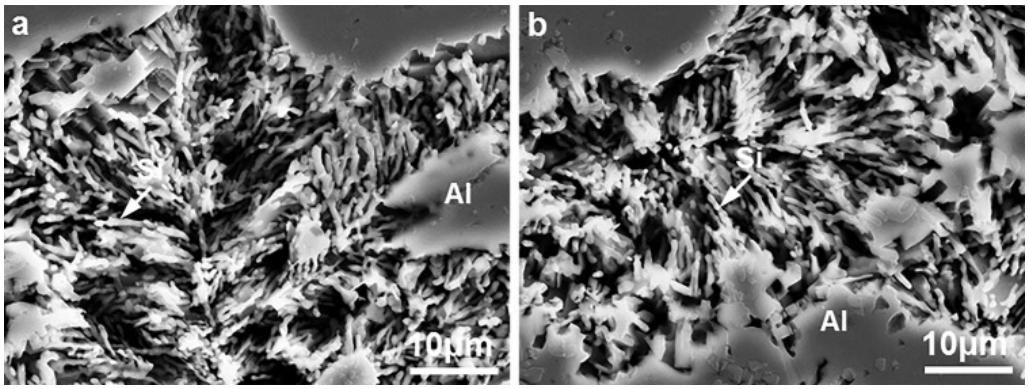

Fig. 4. SEM micrographs showing the morphology of eutectic Si phase in the as–cast A9Si0.45Mg alloys refined by (a) Al5Ti1B and (b) Al3Ti3B after deep etching.

Fig. 5(a) and (b) present the SEM morphology and distribution of intermetallic phases in the as–cast Al9Si0.45Mg alloys refined by Al5Ti1B and Al3Ti3B, separately. Primary α–Al phase, Al–Si eutectic phase and β–Mg2Si intermetallic phase were identified coexisting in the as–cast Al9Si0.45Mg alloys both refined by Al5Ti1B and Al3Ti3B. β–Mg2Si phase is located in the eutectic Al–Si eutectic region, and its size is larger than the eutectic Si phase, as indicated by the arrows in Fig. 5. Obviously, the primary α–Al phase in the as–cast Al9Si0.45Mg alloy refined by Al3Ti3B is also much finer than that refined by Al5Ti1B under the SEM observation.

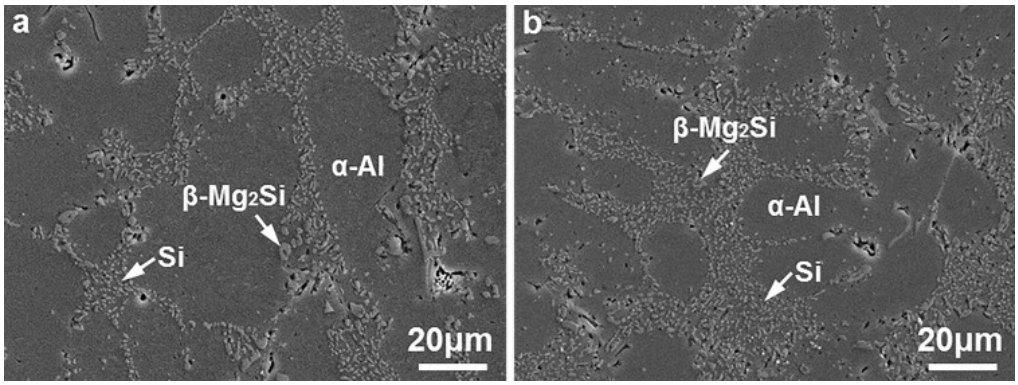

Fig. 5. SEM micrographs showing the morphology and distribution of intermetallic phases in the as–cast Al9Si0.45Mg alloys refined by (a) Al5Ti1B and (b) Al3Ti3B.

3.2. Microstructure after heat treatment

It is well–known that solution treatment can spheroidise the eutectic Si phase and dissolve intermetallic phases to form saturated solid solution [20]. Fig. 6(a) and (b) show the SEM morphology of the eutectic Si phase in the Al9Si0.45Mg alloys refined by Al5Ti1B and

Al3Ti3B, respectively, after solution treatment and aging treatment. The eutectic Si phase shows spheroidal morphology, as indicated by the arrows in Fig. 6, and it is significantly different to the fibrous morphology observed in Fig. 4 under the as–cast condition. The spheroidised Si particles are smaller than 8 μm, and their aspect ratio is smaller than 2.5. The spheroidised fine Si particles with small aspect ratio after heat treatment are capable of improving the mechanical properties [21].

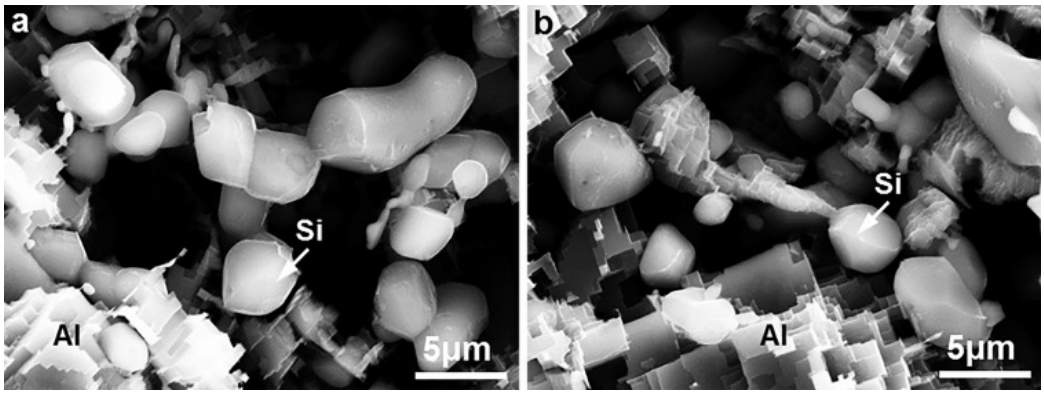

Fig. 6. SEM micrographs showing the morphology of eutectic Si phase in the T6 heat–treated Al9Si0.45Mg alloys refined by (a) Al5Ti1B and (b) Al3Ti3B.

Fig. 7(a) and (b) present the SEM morphology and distribution of the intermetallic phases in the Al9Si0.45Mg alloys refined byAl5Ti1B and Al3Ti3B, separately, after solution treatment and aging treatment. The primary α–Al phase and the spheroidised Si particles were clearly visible, but the β–Mg2Si intermetallic phase was hardly observed in the microstructure both refined by Al5Ti1B and Al3Ti3B, which indicated that the β–Mg2Si intermetallic phase was well dissolved into the α–Al matrix after the solution treatment. The saturated solid solution could ensure the precipitation of nanoscale strengthening precipitates in the α–Al matrix after aging treatment, which contributes to the strengthening of the alloy after T6 heat treatment. The spheroidised Si particles in the heat–treated alloys refined by Al5Ti1B and Al3Ti3B are much similar to each other. Similar to the as–cast condition, the primary α–Al phase in the T6 heat–treated Al9Si0.45Mg alloy refined by Al3Ti3B is also much finer than that refined by Al5Ti1B, since T6 heat treatment hardly has any effect on the size of the primary α–Al phase.

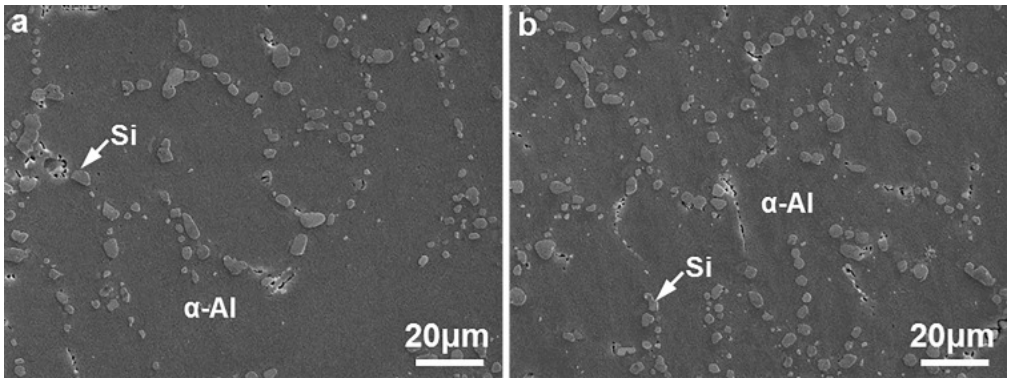

Fig. 7. SEM micrographs showing the morphology and distribution of intermetallic phases in the T6 heat–treated Al9Si0.45Mg alloys refined by (a) Al5Ti1B and (b) Al3Ti3B.

3.3. Mechanical properties after heat treatment

The Al9Si0.45Mg alloy is heat treatment strengthening alloy and mainly used after heat treatment, so its mechanical properties after heat treatment were focused. Fig. 8(a) shows the tensile stress–strain curves of the Al9Si0.45Mg alloys under the three grain refinement condition, after T6 heat treatment. From Fig. 8(a), the Al3Ti3B refined alloy has both higher strength and ductility than the non–refined and Al5Ti1B refined alloys. Fig. 8(b) presents the tensile properties of the T6 heat–treated Al9Si0.45Mg alloys. The yield strength (YS), ultimate tensile strength (UTS) and elongation (El) of the non–refined alloy are 298 ± 2 MPa, 350 ± 2 MPa and 4.5 ± 0.7% respectively. The Al5Ti1B refined alloy provides the YS of 304 ± 2 MPa and the UTS of 357 ± 3 MPa, and the El of 8.0 ± 1.0%. The Al3Ti3B refined alloy provides the YS of 311 ± 1 MPa, the UTS of 366 ± 1 MPa and the El of 11.1 ± 1.2%. It is clear that the strength could be increased, and the elongation could be significantly increased by 38.8% in the Al3Ti3B refined alloy, when compared with the Al5Ti1B refined alloy.

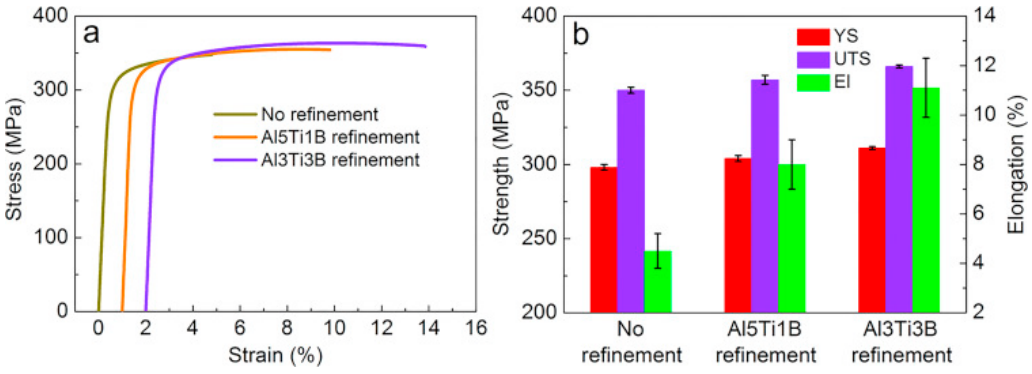

Fig. 8. (a) Representative tensile stress–strain curves and (b) tensile properties of the Al9Si0.45Mg alloys under different grain refinement condition after T6 heat treatment.

4. Discussion

4.1. Precipitation strengthening

Fig. 9 presents the TEM micrographs taken along the <001>Al axis showing precipitate in the Al9Si0.45Mg alloy after T6 heat treatment. Fig. 9(a) shows the bright field image of precipitate in the α–Al matrix, embedded β" precipitate and lying β" precipitate were found in the α–Al matrix when observed along <001>Al axis, which indicates that the β" precipitate is needle–like, and the embedded β" precipitate and lying β" precipitate were the same β" precipitate in nature. Fig. 9(b) shows the SADP of α–Al matrix and β" precipitates in Fig. 9(a), the bright points are diffraction points of the α–Al matrix, while the grey cross lines between the bright points are diffraction patterns of β" precipitates, which indicates that the β" precipitates are in the metastable state and the heat–treated alloy is in the peak strength state. Fig. 9(c) shows the HRTEM image of the β" precipitate embedded in the (001)Al plane, and it clearly presents the unit cell of C–centered monoclinic structure with a = 1.52 nm and c = 0.67 nm, which verifies

that the embedded precipitate is β" [22,23]. Fig. 9(d) shows the corresponding FFT patterns of the rectangle area in Fig. 9(c), and it also confirms that the embedded precipitate is β". Fig. 9(e) shows the HRTEM image of the β" precipitate lying on the (001)Al plane, and Fig. 9(f) shows the corresponding FFT patterns of the rectangle area in Fig. 9(e), which verifies that the lying precipitate is β", and the β" precipitate is fully coherent with the α–Al matrix along the b-axis. As reported in literatures [24,25], the needle–like β" precipitate provides peak strengthening of the T6 heat–treated Al–Si–Mg alloy, which contributes to the high yield strength of above 300 MPa of the Al9Si0.45Mg cast alloy after T6 heat treatment.

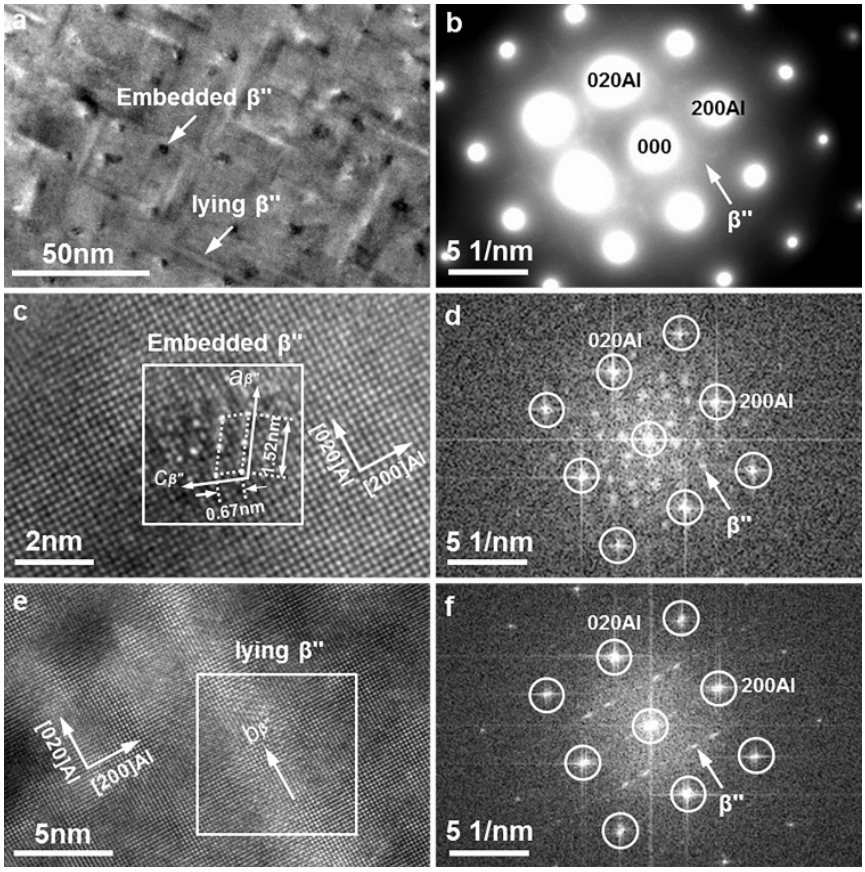

Fig. 9. TEM micrographs taken along the <001>Al axis showing the β" precipitate in the T6 heat–treated Al9Si0.45Mg alloy, (a) bright field image, (b) SADP of (a), (c) HRTEM image of embedded β" precipitate, (d) FFT pattern of (c), (e) HRTEM image of lying β" precipitate and (f) FFT pattern of (e).

4.2. Effects of grain refinement on microstructure

Fig. 10(a) shows the XRD patterns of the Al5Ti1B master alloy used for refinement in this article, TiAl3 and TiB2 particles were found coexisting in the Al5Ti1B master alloy. It has been well documented that the particles introduced into the melt through the addition of Al5Ti1B grain refiner are the soluble TiAl3 and the insoluble TiB2 particles, which is consistent with the XRD results in Fig. 10(a). The TiB2 particles that act as heterogeneous nucleation sites could be poisoned by Si by coating the surfaces with Ti–Si compounds [26]. The dissolved Ti from TiAl3 particles, which also contributes to grain refinement under Al5Ti1B by slowing down the growth of the freshly formed a–Al crystals while partitioning between the solid and

liquid phases, is also rendered ineffective as it also forms Ti–Si compounds and precipitates out of the melt. It has been reported that solute Ti hardly offers any grain refinement effect in Al–Si alloys with 7 wt% Si [27]. The Al9Si0.45Mg cast alloy contains a high level of Si at 9 wt%, so the poisoning effect of TiB2 particles is significant, and the solute Ti might hardly provide growth restriction for the primary α–Al phase, due to the formation of Ti–Si compounds, which results in the coarse primary α–Al grains of 646 ± 155 in the alloy refined by Al5Ti1B.

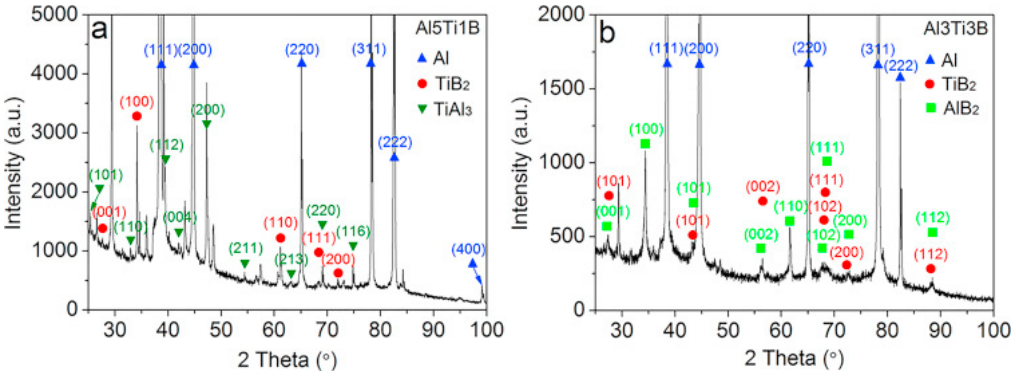

Fig. 10. X-ray diffraction patterns of (a) Al5Ti1B and (b) Al3Ti3B master alloys used for grain refinement.

Fig. 10(b) shows the XRD patterns of the Al3Ti3B master alloy used for refinement in this article, TiB2 and AlB2 particles were found coexisting in the master alloy, while no TiAl3 particles were found. AlB2 particles could also act as heterogeneous nucleation sites for α–Al [15], thus the XRD results indicate that the Al3Ti3B grain refiner does not supply soluble TiAl3 particles (solute Ti), and relies only on the insoluble AlB2 and TiB2 borides to promote heterogeneous nucleation. Borides in the Al3Ti3B grain refiner are nearly three times as many as that in Al5Ti1B, since the B content dictates the population of boride particles. This was also evidenced by the B content listed in Table 1. Moreover, it is reported that more than half of the boride particles in the Al3Ti3B grain refiner are the AlB2 variety [15]. Therefore, the performance of the Al3Ti3B for the refinement of the high silicon Al9Si0.45Mg cast alloy is clearly superior with respect to that of Al5Ti1B, with the decrease of size of the primary α–Al grain to 326 ± 116 μm, as shown in Fig. 3. The AlB2 particles are credited for this improvement since the TiB2 particles suffer from Si poisoning.

4.3. Effects of grain refinement on strength and ductility

Generally, the strength of cast aluminium alloys is decided by grain size strengthening, secondary phase strengthening, solution strengthening, precipitate strengthening and strain strengthening. So the strength of the T6 heat–treated Al9Si0.45Mg cast alloys is dependent on the grain size of primary α–Al phase, the spheroidised secondary Si phase and the β" precipitation phase in the α–Al matrix. From Fig. 7, the spheroidised Si particles in the Al5Ti1B and Al3Ti3B refined alloys are much similar to each other. Moreover, it was found that there was no difference for the β" precipitation phase in the α–Al matrix of Al5Ti1B and Al3Ti3B refined alloys by TEM observation. Thus when compared with the Al5Ti1B refined alloy, the increase of strength in the Al3Ti3B refined alloy can be solely attributed to better grain refinement of the primary α–Al phase. When the grain size is above the nanoscale, it is well

known that the relation between yield strength and grain size for structure materials can be described mathematically by the Hall–Petch equation

$\sigma y=\sigma 0+kd$

Where σy (MPa) is the yield strength, σ0 is a material constant for the starting stress for dislocation movement, k is the strengthening coefficient, and d (μm) is the grain diameter.

From Fig. 3, the experimental grain size (d) of the primary α–Al phase in the non–refined, Al5Ti1B refined and Al3Ti3B refined Al9Si0.45Mg alloys are 1288 ± 361 μm, 645 ± 146 μm and 326 ± 116 μm respectively. As shown in Fig. 8, the corresponding experimental yield strength (σy) of the non–refined, Al5Ti1B refined and Al3Ti3B refined Al9Si0.45Mg alloys are 298 ± 2 MPa, 304 ± 2 MPa and 311 ± 1 MPa separately, after T6 heat treatment. Based on the three experimental grain size and corresponding yield strength, the relation between the yield strength and grain size of the T6 heat–treated Al9Si0.45Mg alloy was well fitted linearly as σy = 285.1 + 470.2·d−1/2, as plotted in Fig. 11, and the fitting errors for the intercept and slope are 1.0 (0.4%) and 23.4 (5.0%) respectively, which indicates that the relation between the yield strength and grain size of the T6 heat–treated Al9Si0.45Mg alloy conforms to the Hall–Petch relation. According to Eq. (1), the decrease in grain size will result in the increase of yield strength, which leads to the increase of yield strength of the heat–treated alloy by 7 MPa to 311 ± 1 MPa under the refinement of Al3Ti3B, when compared with the condition that refined by Al5Ti1B.

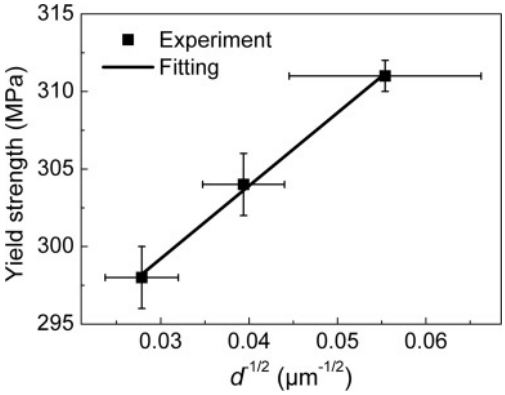

Fig. 11. Hall–Petch relation between the yield strength and grain size (d) of the T6 heat–treated Al9Si0.45Mg alloy.

Fig. 12(a) and (c) show the low magnification SEM fracture morphology of the T6 heat–treated Al9Si0.45Mg cast alloy refined by Al5Ti1B and Al3Ti3B, respectively. Fig. 12(b) shows the enlarged SEM fracture morphology of the area marked by the rectangle in Fig. 12(a), which reveals that the fracture of the Al5Ti1B refined alloy comprises uniform distributed Al dimples and cracked Si, and the cracked Si was verified by EDS analysis, as shown in Fig. 12(a). Fig. 12(d) shows the enlarged SEM fracture morphology of the Al3Ti3B refined alloy, which is very similar to that of the Al5Ti1B refined alloy, with uniform distributed Al dimples and cracked Si present, and the cracked Si was also confirmed by EDS analysis, as shown in Fig. 12(c). It has been claimed that all the cracks seen in Si are because the material has formed on a double oxide which has a crack in its centre, which would explain the large density of ductile dimples

seen on the fracture surfaces [28]. The reason is that each dimple represents a microscopic oxide defect in a Si particle, allowing the particle to fracture, followed by ductile shearing to form a dimple.

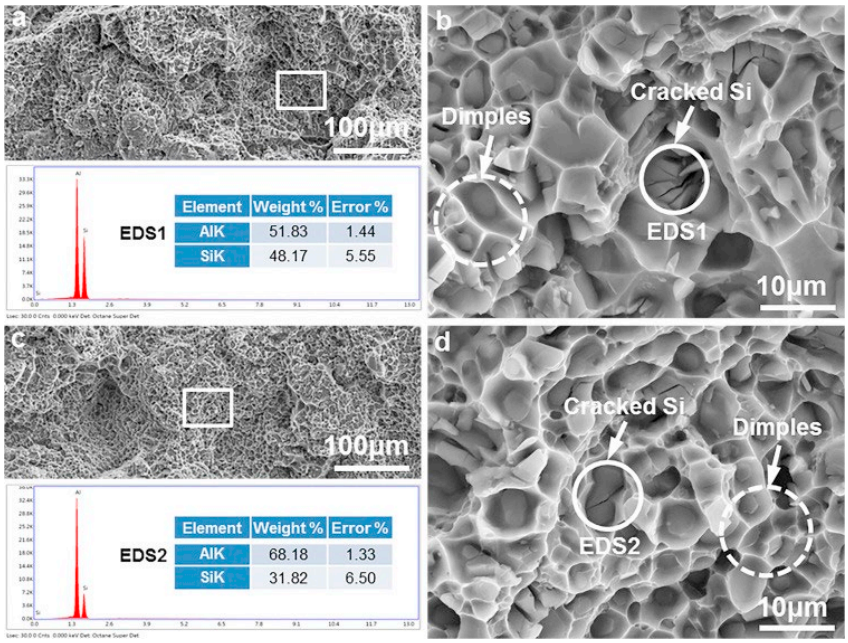

Fig. 12. SEM images showing fracture morphology in the T6 heat–treated Al9Si0.45Mg alloy refined by (a, b) Al5Ti1B and (c, d) Al3Ti3B with (a, c) low magnification and (b, d) high magnification.

Generally, the ductility of cast aluminium alloys is dependent on defects, the primary phase, the secondary phase and strength. From Fig. 7, the spheroidised secondary Si particles in the Al5Ti1B and Al3Ti3B refined alloys are much similar to each other both in size and shape. Moreover, for structural materials, the increase in strength is inevitably sacrificed by the reduction in ductility, which is known as the strength–ductility trade–off dilemma [29]. As shown in Fig. 8, the strength of the Al3Ti3B refined alloy is higher than that of the Al5Ti1B refined alloy, so the increase of strength in Al3Ti3B refined alloy should contribute to the decrease of ductility, from the view point of strength and strength–ductility trade–off dilemma. However, the ductility of the Al3Ti3B refined alloy is significantly higher than that of the Al5Ti1B refined alloy. Thus the ductility of the T6 heat–treated Al9Si0.45Mg cast alloys is mainly controlled by defects and the primary α–Al phase.

According to Campbell′ s theory, the bi ‐ film oxides controlled the failure properties of cast aluminium alloys, the precipitation of inoculation particles from the addition of Al ‐ Ti ‐ B grain refiners can sediment oxides in the melt before pouring into the mould, which will reduce the content of oxides in the casting, and that is beneficial to the ductility of cast aluminium alloys, since crack is easy to start from the oxides defect [28]. As described in the experimental section, after adding the Al5Ti1B or Al3Ti3B master alloy, the melt was hold for 10 min before

the first pouring, and eight castings were made one after one in 20 min, so the sedimentation time of oxides after addition of grain refiners and before pouring was from 10 min to 27.5 min for the eight continuous casting, which is enough for the sedimentation of oxides. Moreover, the sediment was carefully undisturbed during the pour. As discussed in Section 4.2, the inoculated particles under the addition of Al3Ti3B grain refiner were nearly three times as many as that of the Al5Ti1B condition, so the sedimentation of oxides under the refinement of Al3Ti3B was significantly superior to that under the refinement of Al5Ti1B. Thus the content of oxides in the Al3Ti3B refined alloy is lower than that of the Al5Ti1B refined alloy, which contributes to the improvement of ductility in the Al3Ti3B refined alloy, when compared with the Al5Ti1B refined alloy.

Statistical results showed that the area percentage of porosity defect in the Al5Ti1B refined alloy was 0.11 ± 0.03%, while the area percentage of porosity in the Al3Ti3B refined alloy was decreased significantly to 0.02 ± 0.01%. It is also well known that crack is easy to start from the porosity defect [30], so the significant decrease of porosity defect also contributes to the increase of ductility in the Al3Ti3B refined alloy, when compared with the Al5Ti1B refined alloy. As shown in Fig. 3, the grain size of the primary α–Al phase in the Al3Ti3B refined alloy is reduced by 49.5%, when compared with the Al5Ti1B refined alloy, so the number and area of grain boundary in the Al3Ti3B refined alloy are larger in the Al3Ti3B refined alloy comparing with the Al5Ti1B refined alloy. After the formation of crack source from the oxides and porosity defects, the crack will propagate from the crack source to the whole fracture section. The increased number and area of grain boundary in the Al3Ti3B refined alloy will be more efficient in impeding the propagation of crack, which contributes to the increase of ductility as well, when compared with the Al5Ti1B refined alloy. Thus the increase of ductility in the Al3Ti3B refined alloy resulted from the reduced oxides and porosity defects as well as the decreased grain size of the primary α–Al phase, when compared with the Al5Ti1B refined alloy.

5. Conclusions

(1) Al3Ti3B can significantly refine the primary α–Al grains in the high silicon Al9Si0.45Mg cast alloy. Al3Ti3B is more effective than Al5Ti1B for the grain refinement of the Al9Si0.45Mg alloy. The grain sizes of primary α–Al phase are 1288 ± 361 μm and 645 ± 146 μm in the non–refined and Al5Ti1B refined alloys respectively, and that is decreased significantly to 326 ± 116 μm in the Al3Ti3B refined alloy.

(2) Both the strength and ductility are increased in the T6 heat–treated Al9Si0.45Mg cast alloy refined by Al3Ti3B, when compared with the non–refined and Al5Ti1B refined alloy. The yield strength, ultimate tensile strength and elongation of the non–refined alloy are 298 ± 2 MPa, 350 ± 2 MPa and 4.5 ± 0.7% separately. With the change of grain refiner from Al5Ti1B to Al3Ti3B, the yield strength is increased from 304 ± 2 MPa to 311 ± 1 MPa, and the ultimate tensile strength is increased from 357 ± 3 MPa to 366 ± 1 MPa, while the elongation is increased significantly by 38.8% from 8.0 ± 1.0% to 11.1 ± 1.2%.

(3) Primary α–Al phase, Al–Si eutectic phase and β–Mg2Si intermetallic phase coexist in the as–cast Al9Si0.45Mg cast alloy, and β" phase is precipitated from the α–Al matrix for the peak strengthening of the T6 heat–treated Al9Si0.45Mg alloy. The Hall–Petch relation between the yield strength and grain size of the T6 heat–treated Al9Si0.45Mg cast alloy was determined as $\sigma y = 285.1 + 470.2 \cdot d^{-1/2}$.

(4) TiB2 and TiAl3 particles coexist in the Al5Ti1B master alloy, while TiB2 and AlB2 particles coexist in the Al3Ti3B master alloy. The inoculation of AlB2 particles under Al3Ti3B results in the significant grain refinement of the high silicon Al9Si0.45Mg cast alloy. The increase of strength in the Al3Ti3B refined alloy is attributed to the refinement of the primary α–Al grains, while the increase of ductility in the Al3Ti3B refined alloy resulted from the reduced oxides and porosity defects as well as the decreased grain size.

Acknowledgements

Financial support from Innovate UK under project 131817 is gratefully acknowledged. It is grateful to the reviewer for the introduction of the bi-film theory.

References

[1] M. Javidani, D. Larouche Application of cast Al–Si alloys in internal combustion engine components Int. Mater. Rev., 59 (2014), pp. 132-158

[2] X.X. Dong, L.J. He, G.B. Mi, P.J. Li Two directional microstructure and effects of nanoscale dispersed Si particles on microhardness and tensile properties of AlSi7Mg melt-spun alloy J. Alloy Compd., 618 (2015), pp. 609-614

[3] X.X. Dong, L.J. He, X.S. Huang, P.J. Li Coupling analysis of the electromagnetic transport of liquid aluminum alloy during casting J. Mater. Process. Technol., 222 (2015), pp. 197-205

[4] H.E. Boyer, T.L. Gall Metals Handbook Desk Edition American Society for Metals, Metals Park, Ohio (1985)

[5] Y. Birol AlB3 master alloy to grain refine AlSi10Mg and AlSi12Cu aluminium foundry alloys J. Alloy Compd., 513 (2012), pp. 150-153

[6] Y.F. Han, K. Li, J. Wang, D. Shu, B.D. Sun Influence of high-intensity ultrasound on grain refining performance of Al–5Ti–1B master alloy on aluminium Mater. Sci. Eng. A, 405 (2005), pp. 306-312

[7] M.A. Easton, D.H. Stjohn A model of grain refinement incorporating alloy constitution and potency of heterogeneous nucleant particles Acta Mater., 49 (2001), pp. 1867-1878

[8] X.X. Dong, L.J. He, P.J. Li Gradient microstructure and multiple mechanical properties of AlSi9Cu alloy ribbon produced by melt spinning J. Alloy Compd., 612 (2014), pp. 20-25

[9] J.G. Jung, S.H. Lee, J.M. Lee, Y.H. Cho, S.H. Kim, W.H. Yoon Improved mechanical properties of near-eutectic Al-Si piston alloy through ultrasonic melt treatment Mater. Sci. Eng. A, 669 (2016), pp. 187-195

[10] Y. Birol Production of Al–Ti–B grain refining master alloys from B2O3 and K2TiF6 J. Alloy Compd., 443 (2007), pp. 94-98

[11] P.T. Li, X.G. Ma, Y.G. Li, J.F. Nie, X.F. Liu Effects of trace C addition on the microstructure and refining efficiency of Al–Ti–B master alloy J. Alloy Compd., 503 (2010), pp. 286-290

[12] D. Qiu, J.A. Taylor, M.X. Zhang, P.M. Kelly A mechanism for the poisoning effect of silicon on the grain refinement of Al–Si alloys Acta Mater., 55 (2007), pp. 1447-1456

[13] S.A. Kori, B.S. Murty, M. Chakraborty Development of an efficient grain refiner for Al–7Si alloy and its modification with strontium Mater. Sci. Eng. A, 283 (2000), pp. 94-104

[14] Y. Birol A novel Al–Ti–B alloy for grain refining Al–Si foundry alloys J. Alloy Compd., 486 (2009), pp. 219-222

[15] Y. Birol Performance of AlTi5B1, AlTi3B3 and AlB3 master alloys in refining grain structure of aluminium foundry alloys Mater. Sci. Technol., 28 (2012), pp. 481-486

[16] E. Samuel, B. Golbahar, A.M. Samuel, H.W. Doty, S. Valtierra, F.H. Samuel Effect of grain refiner on the tensile and impact properties of Al–Si–Mg cast alloys Mater. Des., 56 (2014), pp. 468-479

[17] P.T. Li, S.D. Liu, L.L. Zhang, X.F. Liu Grain refinement of A356 alloy by Al–Ti–B–C master alloy and its effect on mechanical properties Mater. Des., 47 (2013), pp. 522-528

[18] P. Tang, W.F. Li, K. Wang, J. Du, X.Y. Chen, Y.J. Zhao, W.Z. Li Effect of Al-Ti-C master alloy addition on microstructures and mechanical properties of cast eutectic Al-Si-Fe-Cu alloy Mater. Des., 115 (2017), pp. 147-157

[19] C. Xu, W.L. Xiao, S. Hanada, H. Yamagata, C.L. Ma The effect of scandium addition on microstructure and mechanical properties of Al-Si-Mg alloy: a multi-refinement modifier Mater. Charact., 110 (2015), pp. 160-169

[20] M. Tiryakioğlu Si particle size and aspect ratio distributions in an Al–7%Si–0.6%Mg alloy during solution treatment Mater. Sci. Eng. A, 473 (2008), pp. 1-6

[21] C. Xu, W.L. Xiao, R.X. Zheng, S. Hanada, H. Yamagata, C.L. Ma The synergic effects of Sc and Zr on the microstructure and mechanical properties of Al-Si-Mg alloy Mater. Des., 88 (2015), pp. 485-492

[22] S.J. Andersen, H.W. Zandbergen, J. Jansen, C. Traeholt, U. Tundal, O. Reiso The crystal structure of the β" phase in Al–Mg–Si alloys Acta Mater., 46 (1998), pp. 3283-3298

[23] W.C. Yang, M.P. Wang, R.R. Zhang, Q. Zhang, X.F. Sheng The diffraction patterns from β" precipitates in 12 orientations in Al–Mg–Si alloy Scr. Mater., 62 (2010), pp. 705-708

[24] W.C. Yang, L.P. Huang, R.R. Zhang, M.P. Wang, Z. Li, Y.L. Jia, R.S. Lei, X.F. Sheng Electron microscopy studies of the age-hardening behaviors in 6005A alloy and microstructural characterizations of precipitates J. Alloy Compd., 514 (2012), pp. 220-233

[25] W.C. Yang, S.X. Ji, L.P. Huang, X.F. Sheng, L. Zhou, M.P. Wang Initial precipitation and hardening mechanism during non-isothermal aging in an Al-Mg-Si-Cu 6005A alloy Mater. Charact., 94 (2014), pp. 170-177

[26] P.S. Mohanty, J.E. Gruzleski Grain refinement mechanisms of hypoeutectic Al-Si alloys Acta Metall. Mater., 44 (1996), pp. 3749-3760

[27] Y. Birol Effect of silicon content in grain refining hypoeutectic Al-Si foundry alloys with boron and titanium additions Mater. Sci. Technol., 28 (2012), pp. 385-389

[28] J. Campbell Complete Casting Handbook: Metal Casting Processes, Metallurgy, Techniques and Design (second ed), Elsevier Ltd, Oxford (2015)

[29] R.O. Ritchie The conflicts between strength and toughness Nat. Mater., 10 (2011), pp. 817-822

[30] X.X. Dong, L.J. He, X.S. Huang, P.J. Li Effect of electromagnetic transport process on the improvement of hydrogen porosity defect in A380 aluminum alloy Int. J. Hydrog. Energy, 40 (2015), pp. 9287-9297